5-2022

# Synthesis and characterization of ternary Pt nanoally catalysts for fuel cells

Ylith Peck
*Binghamton University--SUNY*, ypeck1@binghamton.edu

# SYNTHESIS AND CHARACTERIZATION OF TERNARY PT NANOALLOY CATALYSTS FOR FUEL CELLS

YLITH PECK

STATE UNIVERSITY OF NEW YORK AT BINGHAMTON, 2022

HONOR THESIS

Submitted in partial fulfilment of the requirements for Distinguished Independent Work in Chemistry in the Harpur College of Binghamton University, State University of New York

2022

Accepted in partial fulfillment of the requirements for Distinguished Independent Work in Chemistry

State University of New York at Binghamton

2022

Dr. Chuan-Jian Zhong May 6, 2022

Advisor, Department of Chemistry

Dr. Alistair J. Lees May 6, 2022

Department of Chemistry

Dr. John Swierk May 6, 2022

Department of Chemistry

**ABSTRACT**

A hydrogen fuel cell is an electrochemical device that converts oxygen and hydrogen into electrical energy while producing water as the only by-product, which has attracted growing interest, especially in the automotive industry. This technology is efficient and has zero pollution to the environment, in contrast to the direct use of fossil fuels in combustion engines which produce pollution and greenhouse gas emissions. One of the key components for hydrogen fuel cells is the catalyst that operates at the cathode, which currently use platinum. Due to the scarce amount of platinum in the world, the manufacturing cost for fuel cells is high. This is one of the main reasons why fuel cell vehicles are not widely commercialized. In order to address the high cost of platinum, one of the approaches is to alloy different transition metals such as iron and nickel with platinum for the preparation of the catalysts. This thesis work has investigated different synthesis techniques for the preparation of various ternary nanoalloy catalysts. Characterization of the nanoalloy structures were carried out using X-ray diffraction (XRD) and Inductively Coupled Plasma-Optical Emission Spectrometry (ICP-OES) methods. The XRD results showed a clear dependence of the lattice constants on the ternary composition. ICP results showed the high controllability of the nanoalloys at various compositions. Membrane electrode assembly (MEA) was prepared with selected catalysts, and the catalytic performance was tested in a proton exchange membrane fuel cell. Results will be discussed along with the implication of the findings for the design of low-cost and durable catalysts for fuel cell applications.

## Table of Contents

## 1. INTRODUCTION

As the increasing consumption of non-renewable fossil fuels has taken a toll on our environment through carbon emissions and pollution, scientists have been seeking other energy alternatives to tackle this issue. Amongst these innovative energy alternatives, fuel cells have been able to gain recognition in the auto-mobile industry as a promising way to decrease greenhouse emissions [1]. Greenhouse emissions trap heat and make the planet warmer. This leads to substantial changes in the ecosystem and makes it difficult for many species to survive. According to the United States Environmental Protection Agency (EPA), the greenhouse gas emissions from the transportation sector contributed to 27% of all emissions in 2020, which generates the largest share of emissions, with the electrical grid and industry sectors accounting for the 2$^{nd}$ and 3$^{rd}$ largest polluters [2]. Figure 1 shows U.S. greenhouse gas emissions per economic sector in 2020.

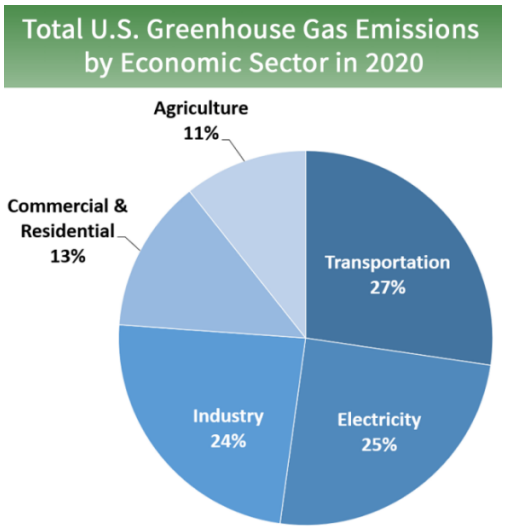


**Figure 1**. Total U.S. greenhouse gas emissions in 2020 by sector. Total emissions 5981 million metric tons of $CO_2$ equivalent.

In the transportation sector, $CO_2$ is the main contributor of greenhouse gas emissions resulting from the combustion of petroleum-based products in internal combustion engines. According to the U.S. Energy Information Administrations (EIA), 18.1 million barrels of petroleum-based products were consumed in 2020, which is the lowest in the past 15 years [3]. Figure 2 illustrates the number of petroleum-based products each sector consumes.

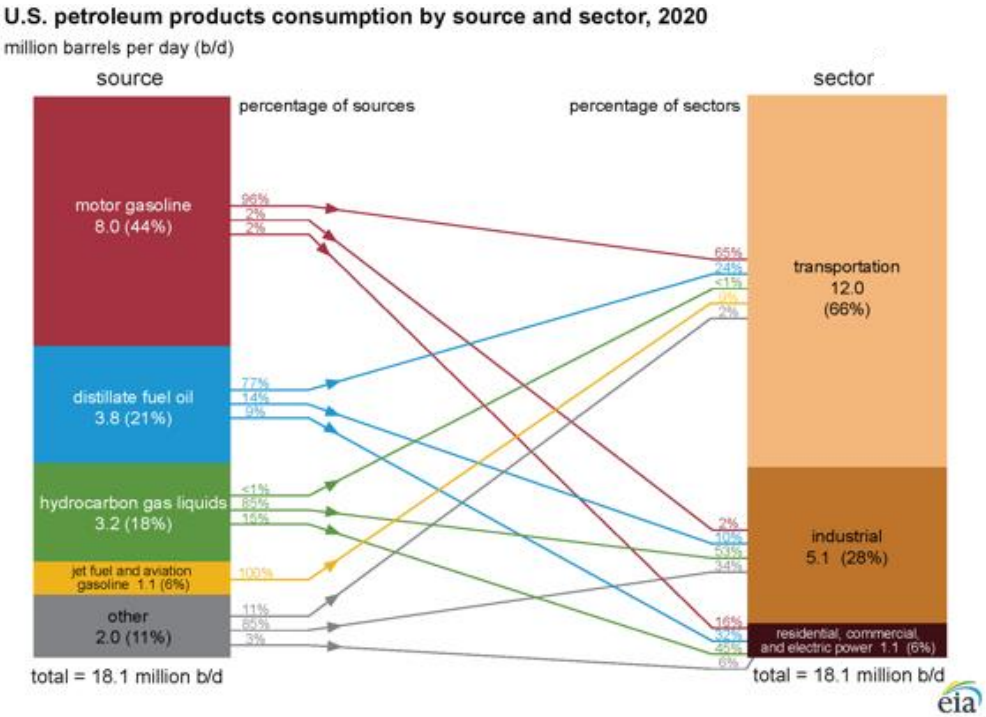


**Figure 2.** U.S. petroleum products consumption by source and sector [3].

The transportation sector consumed 12 million barrels of petroleum-based products in 2020, which means that 66% of all petroleum consumption is due to transportation. To combat carbon emissions from combustion engine vehicles, there is a growing movement to replace these combustion engines with alternative energy engines, with battery electric vehicles being the largest source and fuel cell powered vehicles slowly being introduced into

the economy. Battery electric vehicles are often compared with fuel cell powered vehicles, as both vehicles contribute to the reduction of carbon emission [4]. Although batteries are cheaper and widely assessable, there are inherent disadvantages including the heavy weight of the batteries required in vehicles, the time-consuming recharging cycle, or the reduction in longevity of the battery when speed charging is introduced [5]. Due to these challenges, battery electric vehicles are more suitable for short-distance urban environments. Fuel cells have many advantages over batteries, including high energy density (39.7 kWh $kg^{-1}$), in comparison to the flexible lithium ion batteries (180 Wh $kg^{-1}$), and low recharge rate [6]. Challenges that fuel cells face include the use of expensive metals, like platinum, as catalysts for the Oxygen Reduction Reaction (ORR), platinum poisoning by CO species, and its sluggish kinetics [5].

For large vehicles, such as heavy duty trucks that drive long distances while pulling heavy merchandise, fuel cell engines may be the solution. A fuel cell is an electrochemical cell that converts hydrogen into electricity through redox reactions with oxygen, which means water and electricity are the sole byproducts. For fuel cell vehicles, proton exchange membrane fuel cells (PEMFC) are the primary focus, as shown in Figure 3.

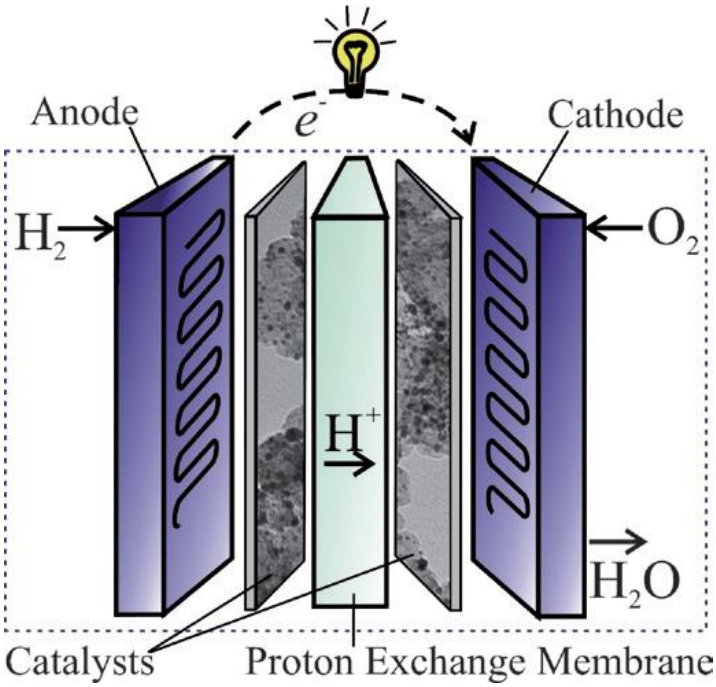


**Figure 3**. Schematic representation of the mechanism of a PEMFC [5].

Hydrogen gas is split into electrons and protons on the anode side, where the protons travel through the Nafion membrane, and the electrons travel through the outside circuit to the cathode. An ORR occurs at the cathode side to form water and energy. The reactions are shown as below:

$$\text{Anode: } H_2 \rightarrow 2H^+ + 2e^- \quad 0.00V$$

$$\text{Cathode: } \frac{1}{2}O_2 + 2H^+ + 2e^- \rightarrow H_2O \; 1.23V$$

$$\text{Overall: } H_2 + \frac{1}{2}O_2 \rightarrow H_2O \; 1.23V$$

At a constant pressure of one atmosphere, the maximum potential of a fuel cell is determined by the Gibbs free energy change in the fuel cell process. Under standard conditions (1 atm and 298K), the maximum potential of a fuel cell is 1.23 V.

Catalysts are an important aspect to ensure the progress of PEMFCs since ORR at the cathode requires catalysts that are stable under an extremely corrosive environment but are still chemically active enough to initiate ORR [7]. Currently, platinum is the most appropriate catalytic material for promoting ORR at the cathode. Due to the high activation barrier in ORR, the addition of a catalyst allows a reaction path with a lower activation barrier to occur. Since this is a catalytic reaction, the platinum is not consumed during the reaction. However, the cost and durability of high loading of platinum have limited the commercialization of fuel cells. In fact, most experts identify the high platinum loading as the most significant barrier to improving the cost and performance of PEMFCs [8]. Researchers have been alloying various metals with platinum in hopes of not only reducing the financial burden of fuel cells, but also increasing the stability and performance of fuel cells. There are multiple methods to produce the platinum base alloy nanocatalysts, which can be simplified into a top-down method and bottom-up method, as shown in Figure 4.

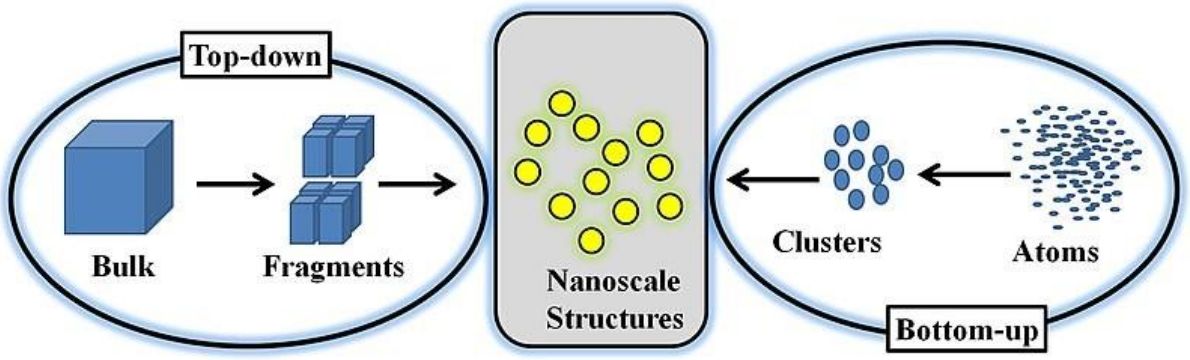


**Figure 4**. Schematic representation of the top-down and bottom-up approach of synthesizing nanocatalysts [9].

The most common bottom-up approach is the wet-chemical synthesis of nanoparticles that involves the chemical reduction of aqueous salt-based metals. This approach has been previously utilized by our group to synthesize various platinum-based nanoparticles. Besides the time-consuming aspect of this approach, the disposal of chemical waste is also costly. Gao *et al.* [10] synthesized high entropy alloy nanoparticles (HEA-NPs) that uniformly disperses the nanoparticles on granular support that utilizes high temperature to create high entropy to prevent phase segregation. Phase segregation gives only a relative degree of alloying as opposed to fully alloying. During the process of the formation of an alloy, the difference between the lattice parameters of the metals creates a phenomenon known as lattice strain [11]. Lattice strain of the catalyst affects the binding strength of O-O bond cleavage in ORR. In the case of Pt-based alloys, the lattice parameter is shortened, causing more strain on the O-O bond cleavage to accelerate the reaction. The alteration of lattice parameters influences the material's physical properties, which can be quantitatively characterized by x-ray diffraction.

Ternary nanoalloys, like PtPdNi, PtNiCo, and PtVCo, or binary nanoparticles like PdCu have previously been synthesized and investigated by our group [12-15]. The syntheses involved the reduction and decomposition of the metal precursors in organic solvent. Although this synthesis method is reliable, one downside is the high cost associated with the disposal of organic waste, and the long experimental process that is time-consuming.

Thus, there are two major problems that must be addressed. The first is the high cost and waste management associated with the use of large amounts of organic solvents in wet chemical synthesis. One approach to addressing the problem is to reduce the metal salts into metallic NPs using hydrogen gas as a reducing agent in the presence of carbon under elevated temperatures. The produced nanoparticles are supported on carbon support without any organic solvents. The precursor metals are grinded with carbon to increase the homogeneity distribution before the thermal treatment. The second problem is the high loading of Pt in the catalysts. One approach to addressing this problem is the synthesis of various binary or ternary alloy catalysts with low Pt composition by alloying Pt with 3d transition metals such as Ni, Co, and Fe. The resulting nanoalloys feature a reduced Pt−Pt bond distance and increased d-orbital vacancies in the platinum 5d orbital. Comprehensive understanding of the synthesis of nanocatalysts is not the only requirement, the physical characterization to better understand the structures, compositions, and phase structure of these NPs are key to determining the catalyst with the highest catalytic activity. In particular, X-ray diffraction (XRD) is employed to characterize the crystalline structures of these NPs synthesized. Our group had previously synthesized PtNiFe with the wet synthesis method [16]. We will compare the physical characteristics and catalytic performance of the PtNiFe NPs synthesized using the solid-state synthesis method and those from previous synthesis techniques to determine the effectiveness of this method. This thesis work will focus on the synthesis of

nanoalloy catalysts by alloying nickel and iron with platinum to reduce the cost and maintaining the controllability of the composition. Solid-state synthesis is employed in this thesis. XRD and ICP-OES is used to analyze the composition and structure of the NPs synthesized. As part of the overall goal of our research, the catalysts will be tested in fuel cells to determine the catalytic performance.

## 2. EXPERIMENTAL METHODS

### 2.1. Chemicals

The required metal precursors to produce PtNiFe NPs were chloroplatinic acid hydrate ($H_2PtCl_6 \cdot H_2O$) $\geq$ 99.9% trace metals basis, Vinyl ferrocene ($C_{12}H_{12}Fe$) 97%, Nickel (II) acetate tetrahydrate ($Ni(OCOCH_3)_2 \cdot 4H_2O$) 98%. Carbon (Vulcan XC-72R) was used for support of the NPs. Each of the chemical precursors was purchased new and used as is without further purification or modification.

### 2.2. Solid-State Synthesis

Various trimetallic PtNiFe NPs with controlled feed compositions were prepared by thermochemical treatment utilizing a solid-state synthesis method. To ensure homogeneous distribution, the metal precursors and carbon support were grinded with a mortar and pestle. The mixture was then placed in a porcelain boat to be heated in a tube furnace

(Lindberg/Blue M) under an atmosphere containing a mixture of hydrogen, 15%, and nitrogen, 85%, supplied from AirGas.

### 2.3. Instrumentation

#### 2.3.1 X-Ray Diffraction (XRD) analysis

X-Ray Diffraction (XRD) is a nondestructive analytical technique that provides information regarding the crystallographic structure. The X-Rays are generated in a cathode ray tube and hit the crystals at specific incident angles. The resulting diffraction from the interaction of the beam with the crystal will change depending on the structure and orientation of the crystal. The diffracted beam is collected by an area detector and can be used with Bragg's Law to identify the structure.

$$2dsin\theta = n\lambda \tag{1}$$

where n is an integer representing the order of diffraction, $\theta$ is Bragg's angle, d is the spacing between the planes, $\lambda$ is the wavelength of the x-ray. Furthermore, the lattice constant can be determined through its cubic relationship with the planes.

$$\frac{1}{d^2} = \frac{h^2 + k^2 + l^2}{a^2} \tag{2}$$

where h, k, and l are the vectors of the space group, and a is the lattice constant.

The Scherrer's equation is used to determine the domain size of the material.

$$\tau = \frac{K\lambda}{Bcos\theta} \tag{3}$$

where $\tau$ the mean size of the ordered domains, K is is a dimensionless shape factor with a value of 0.9 to represent a spherical particle, $\theta$ is Bragg's angle, B is FWHM of the peak, and $\lambda$ is the wavelength of the x-ray beam.

A Phillips X'pert PW 3040 MPD x-ray diffractometer was used to collect XRD data for various compositions of PtNiFe NPs. XRD data was used to analyze the size of this crystal using Cu Kα radiation, with λ=1.5406 Å and the data was collected from 10 to 90° 2θ with a step size of 0.033° and at room temperature.

### 2.3.2 Inductively Coupled Plasma-Optical Emission Spectroscopy technique

Inductively Coupled Plasma-Optical Emission Spectroscopy (ICP-OES) was used to determine the elemental composition of the PtNiFe NPs. This is a technique that analyzes the composition of a solution by directing it through a nebulizer via a peristaltic pump into a spray chamber, and the produced aerosol is led into argon plasma. Atomization and ionization occur where the electrons reach an excited state before dropping down to the ground state and emitting photons. The emission spectrum is measured with a spectrometer, and the light intensity is measured and calculated into a concentration. The samples were prepared with concentrated aqua regia and left to decompose in the solution for 1 hour. After the decomposition, the remaining aqua regia was boiled off. The metallic components left in solution after boiling all the acid were mixed with DI water and left to cool for another hour. Once complete, 10mL of the solution was collected and analyzed.

### 2.3.3 MEA preparation for fuel cell testing

Membrane exchange assemblies (MEAs) were prepared using a hot-pressing method. Pure Pt/C (FuelCellStore 40%) was used for the anode hydrogen oxidation reaction (HOR) catalyst, while the synthesized PtNiFe/C was used for the cathode oxygen reduction reaction (ORR) catalyst. Generally, the catalysts were mixed with Nafion solution (5%) isopropyl alcohol and 18.2MΩ water, this ink was then ultra-sonicated and immediately brush coated onto carbon cloth for the gas diffusion layer (GDL) (CeTech W1S1010) until metal loading between 0.1 – 0.2mg/cm$^2$ was achieved. The electrodes were allowed to dry under ambient conditions over night, then cut into 5cm$^2$ pieces. The electrodes were then sandwiched between Nafion 212 for the proton exchange membrane (PEM) and hot pressed for 5 minutes with heat.

MEA was tested in a working fuel cell system. The prepared MEA was assembled in a fuel cell (Scribner) with active area of 5cm$^2$ and serpentine flow channels and kept at 75°C. The anode was purged with hydrogen gas at 300 scc min$^{-1}$ while the cathode was purged with oxygen gas at 150 scc min$^{-1}$, both gases were held at a backpressure of 30psi. The gases were purged by the ElectroChem Inc, HSA to maintain a temperature of 65°C and 100% humidity. Flow and pressure were controlled using ElectroChem Inc, MTS-A-150. Current and potential was collected using ElectroChem Inc, ECL 150.

## 3. RESULTS AND DISCUSSION

### 3.1 Morphology, Composition and Phase Structure of the PtNiFe Nanoparticle Catalysts

#### 3.1.1 Morphology of PtNiFe Nanoparticles (NP)

PtNiFe/C catalysts with different compositions were synthesized to investigate the physical characteristics and catalytic activity of these catalysts. Contrary to the common wet synthesis process, a solid-state synthesis method was employed. This solid-state synthesis consisted of adding pre-weighed metal precursors and carbon support to a mortar and pestle to grind for 40 minutes. The molar ratio of the metal precursors added is the feed ratio. The mixture is then transferred into a pre-weighed porcelain combustion boat. The boat was placed in the tube heating furnace at 800°C with a 2-hour ramp rate, and a 2.5 hour hold time. A constant flow of hydrogen gas was maintained at 130 mL/min throughout the heating process. It is theorized that the formation of the nanoparticles started with the heat decomposing the metal precursors into metal ions by breaking the bonds between the metal ion and counter ions in the salt. The constant flow of hydrogen gas reduces the surface energy of the metal ions, converting the metal cations to a neutral charge. Aggregates form on the carbon support, and the distance between aggregates prevents the continuation of the aggregation. Figure 5A shows how the NPs look through transmission electron microscopy (TEM).

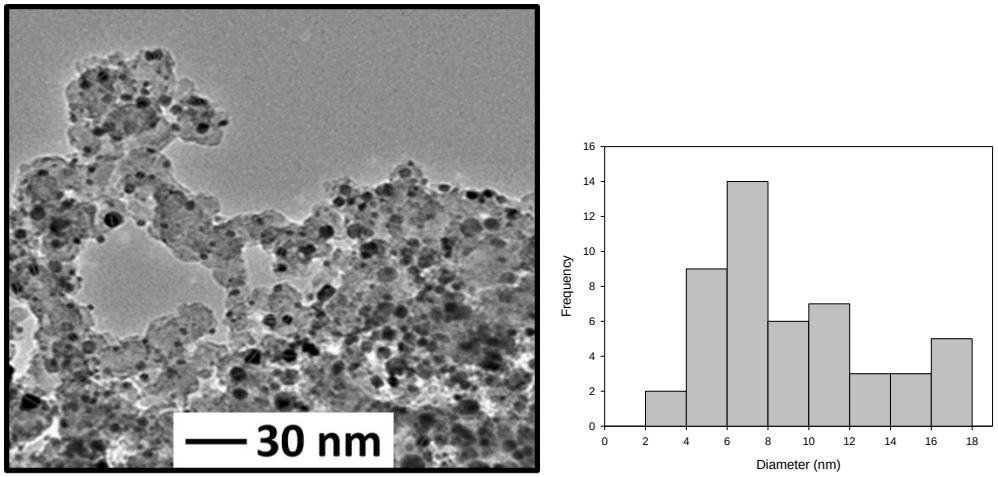


**(A)**

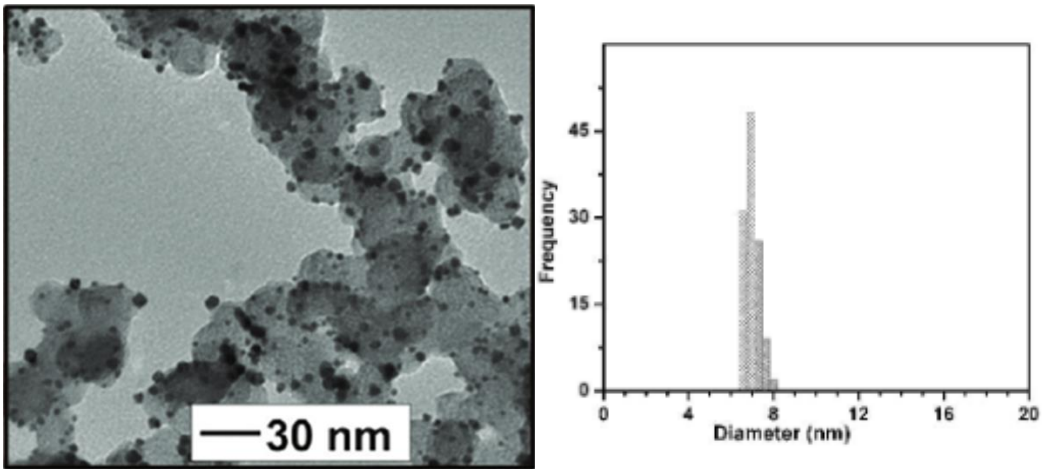


**(B)**

**Figure 5**. (A) TEM of $Pt_{34}Ni_{35}Fe_{31}$ synthesized through solid state synthesis and the size distribution, 7.85±3.81 nm. (B) TEM of $Pt_{46}Ni_{22}Fe_{32}$ /C catalyst synthesized by wet chemical synthesis (7.8 ± 0.6 nm) [16].

These $Pt_{34}Ni_{35}Fe_{31}$ NPs synthesized with wet chemical synthesis (Figure 5B) have an average size of 7.85±3.81 nm. The aggregation size of these NPs is widely varied, with NPs as small as 2 nm to NPs as large as 18 nm. This suggests that while the nanoparticles were formed and exhibit a spherical shape, the standard deviation suggests a multimodal distribution of the particle size. The $Pt_{46}Ni_{22}Fe_{32}$ /C NPs previously synthesized by our group are highly monodispersed round aggregates, with an average size of 7.8±0.6 nm.

### 3.1.2 Composition of PtNiFe Nanoparticles

The main variable in this study is the wide range of different PtNiFe compositions. During the synthesis, an estimated feed ratio of each NP was established based on the molar compositions of the metal precursors weighed. These ratios were merely an estimate, as there may be loss of product during the synthesis process. Thus, the true compositions of the NPs synthesized were identified through ICP-OES, as shown in Table 1.

**Table 1**. Results from ICP-OES composition analysis of the PtNiFe NPs in comparison to the calculated molar feed ratio.

| Molar Feed Ratio | ICP-OES Platinum Composition | ICP-OES Nickel Composition | ICP-OES Iron Composition |
|---|---|---|---|
| $Pt_{11}:Ni_{18}:Fe_{71}$ | 10.7 | 18.4 | 71.0 |
| $Pt_{23}:Ni_{40}:Fe_{37}$ | 24.0 | 45.0 | 31.0 |
| $Pt_{31}:Ni_{27}:Fe_{42}$ | 32.2 | 30.3 | 37.4 |
| $Pt_{41}:Ni_{31}:Fe_{28}$ | 37.3 | 36.4 | 26.2 |
| $Pt_{54}:Ni_{7}:Fe_{39}$ | 55.5 | 8.30 | 36.2 |

The estimated molar feed ratio of each metal aligns closely with the molar feed ratio obtained through ICP-OES. To further examine the correlation, linear regressions of the experimental platinum, nickel, and iron feed ratio as a function of calculated platinum, nickel, and iron feed ratio were established, respectively, as shown in Figure 6 (a-c). A linear regression $y = 0.9982x + 0.0588$ with an $R^2$ value of 0.9801 was established for the platinum feed ratio and composition. A linear regression $y = 1.1547x – 1.0066$ with an $R^2$ value of 0.9936

was established for nickel feed ratio and composition. The linear regression for y = 1.0842x – 6.8562 with an $R^2$ value of 0.9879 for iron feed ratio and composition.

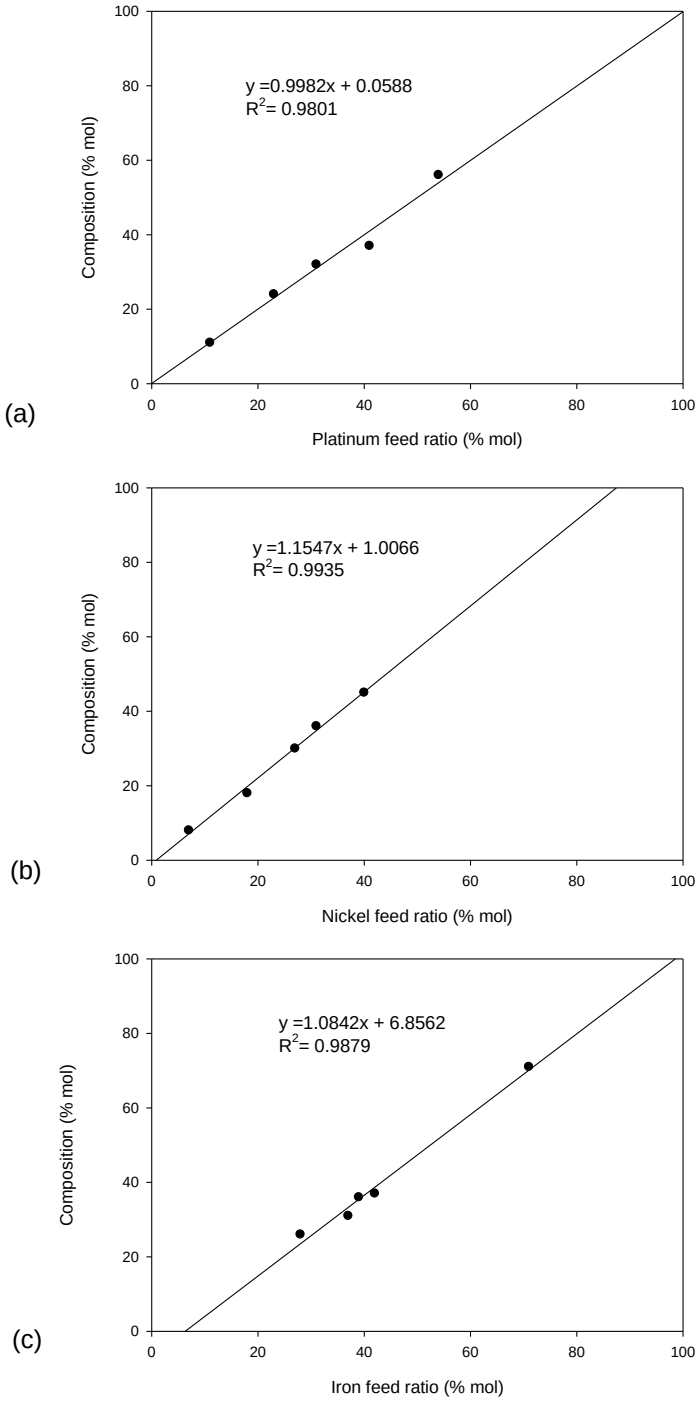


**Figure 6.** Correlation between molar feed ratio and the ICP-OES determined composition in PtNiFe NPs **in terms** of **(a)** platinum, **(b)** nickel**, and (c)** iron.

Based on these linear relationships, a 1:1 ratio of the metal feed ratio and the actual metal composition was established to a high degree of certainty. This is an indication that the solid-state synthesis method is highly controllable in regard to the metal compositions for the metal precursors used during synthesis.

### 3.2 Phase Structure of PtNiFe Nanoparticles

#### 3.2.1 XRD Pattern

To further examine the crystalline properties of the NPs, x-ray diffraction (XRD) was conducted on the five different PtNiFe compositions. Figure 7-11 shows the XRD pattern of $Pt_{11}Ni_{18}Fe_{71}/C$, $Pt_{24}Ni_{45}Fe_{31}/C$, $Pt_{32}Ni_{30}Fe_{37}/C$, $Pt_{37}Ni_{36}Fe_{26}/C$, and $Pt_{56}Ni_{8}Fe_{36}/C$, treated at 800°C under $H_2$. Figure 7 is the XRD pattern of $Pt_{11}Ni_{18}Fe_{71}/C$ exhibiting face-centered cubic (fcc) peaks (111), (200), (220), and (311) at 41.1°, 47.2°, 69.2°, and 83.5°, respectively. At 24.0°, 33.0°, 52.0°, 53.8°, 60.5° and 70.2°, face-centered tetragonal (fct) peaks (001), (110), (002), (201), (112), and (202) are exhibited. The intense peak at 44.2° exhibited a combination of strong fct characteristics and weak fcc characteristics.

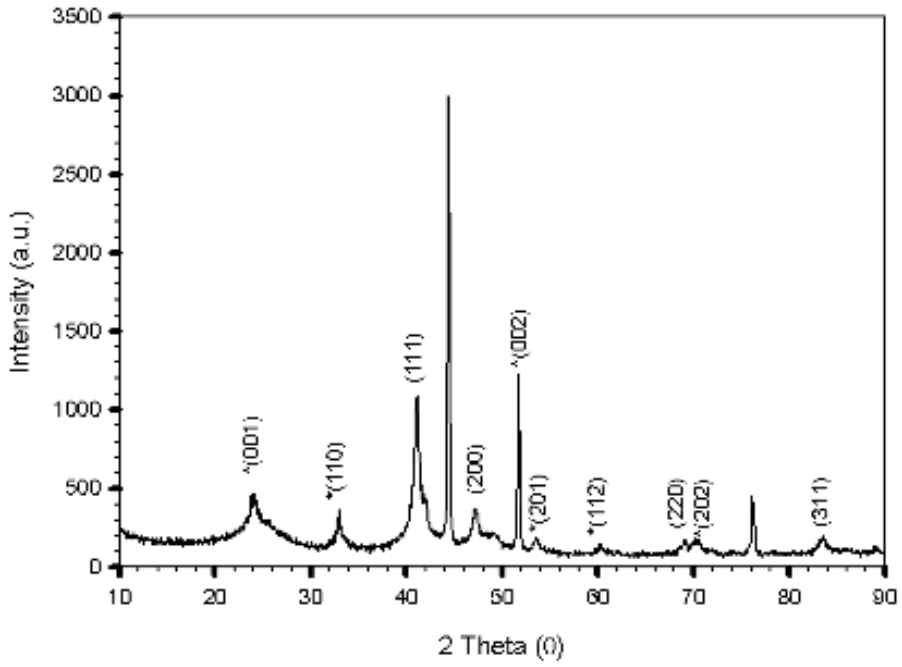


**Figure 7**. XRD pattern of $Pt_{11}Ni_{18}Fe_{71}$/C catalyst prepared by thermochemical treatment at 800°C under $H_2$.

Figure 8 shows the XRD pattern for the next highest concentration of platinum in the PtNiFe NP group. The XRD pattern of $Pt_{24}Ni_{45}Fe_{31}$/C exhibited fcc peaks (111), (200), (220), and (311) at 41.3°, 47.2°, 69.2°, and 84.0°, respectively. At 24.0°, 33.0°, 52.0°, 53.8°, 60.5° and 70.5°, fct peaks (001), (110), (002), (201), (112), and (202) are exhibited. In comparison to the intense peak at 44.2° in $Pt_{11}Ni_{18}Fe_{71}$/C, this peak exhibited more fcc characteristics than fct characteristics.

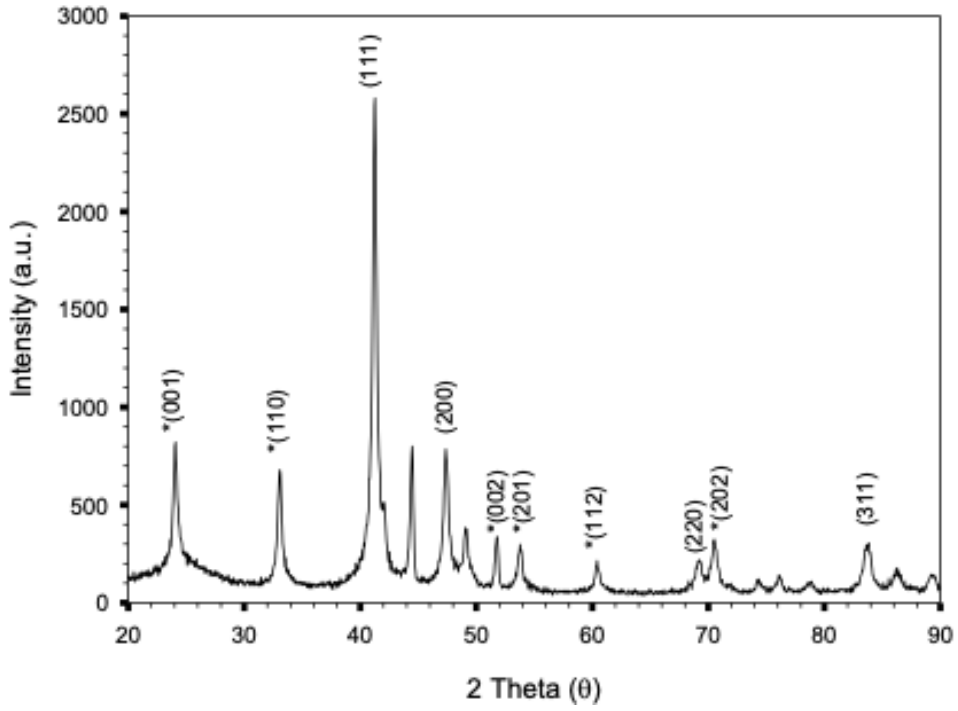


**Figure 8**. XRD pattern of $Pt_{24}Ni_{45}Fe_{31}/C$ catalyst prepared by thermochemical treatment at 800°C under $H_2$.

Figure 9 shows the XRD pattern for the third largest concentration of platinum with the XRD pattern of $Pt_{32}Ni_{30}Fe_{37}/C$ exhibiting fcc peaks of (111), (200), (220), and (311) at 41.2°, 47.2°, 69.2°, and 84.0°, respectively. At 24.0°, 33.0°, 51.8°, 53.8°, 60.5° and 70.5°, fct peaks (001), (110), (002), (201), (112), and (202) are exhibited. The peak at 44.2° is less intense than $Pt_{11}Ni_{18}Fe_{71}/C$, and $Pt_{24}Ni_{45}Fe_{31}/C$, with more fcc characteristics than fct characteristics. This suggests that the concentration of platinum has an impact on the peak at 44.2°

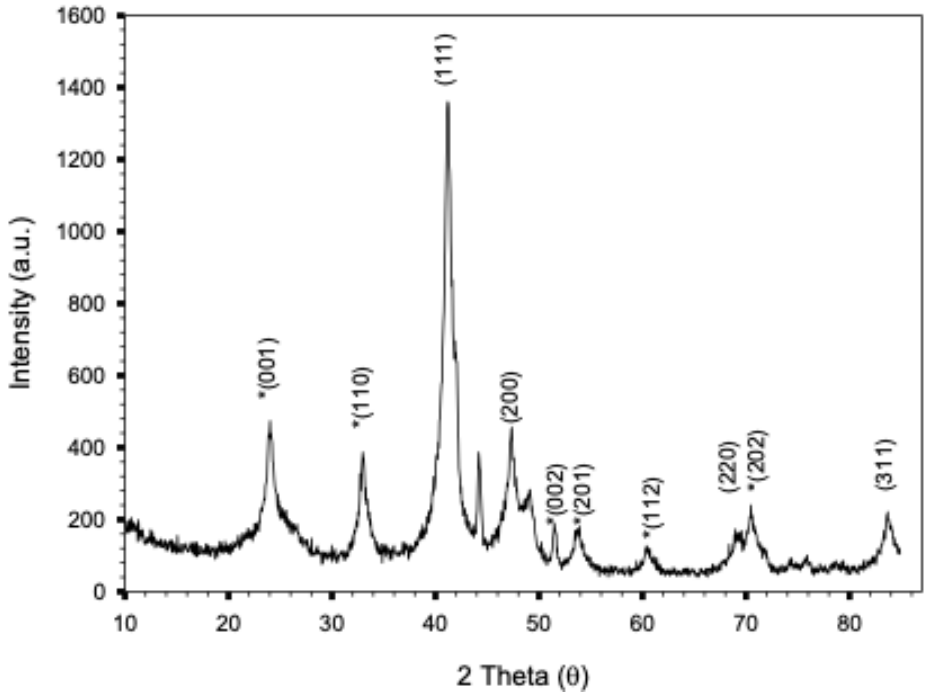


**Figure 9**. XRD pattern of $Pt_{32}Ni_{30}Fe_{37}$/C catalyst prepared by thermochemical treatment at 800°C under $H_2$.

The XRD pattern for the fourth highest concentration of platinum in the PtNiFe group is shown in Figure 10. The XRD pattern of $Pt_{37}Ni_{36}Fe_{26}$/C, exhibited fcc peaks (111), (200), (220), and (311) at 42.0°, 48.0°, 69.5°, and 84.0°, respectively. At 24.0°, 33.0°, 49.8°, 54.0°, 60.7° and 72.0°, fct peaks (001), (110), (002), (201), (112), and (202) are exhibited. There is still a very subtle peak at 44.2°, but nearly negligible compared to the three previous patterns.

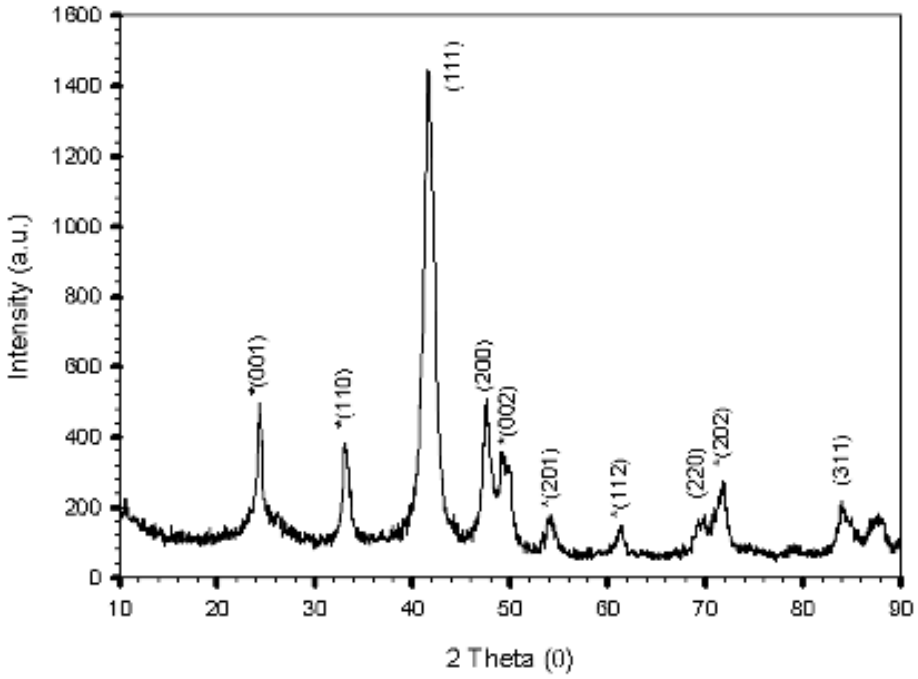


**Figure 10**. XRD pattern of $Pt_{37}Ni_{36}Fe_{26}/C$ catalyst prepared by thermochemical treatment at 800°C under $H_2$

The XRD pattern for the catalyst with the highest concentration of platinum is represented in Figure 11. The XRD pattern of $Pt_{56}Ni_8Fe_{36}/C$ exhibited fcc peaks (111), (200), (220), and (311) at 41.1°, 47.5°, 69.5°, and 83.5°, respectively. At 24.0°, 33.0°, 49.0°, 53.5°, 60.7° and 70.5°, fct peaks (001), (110), (002), (201), (112), and (202) are exhibited. There is no peak at 44.2°, which is an indication of a complete alloy. This strongly suggests that the concentration of platinum in PtNiFe NPs synthesized using the solid-state technique influences the presence of the peak at 44.2°.

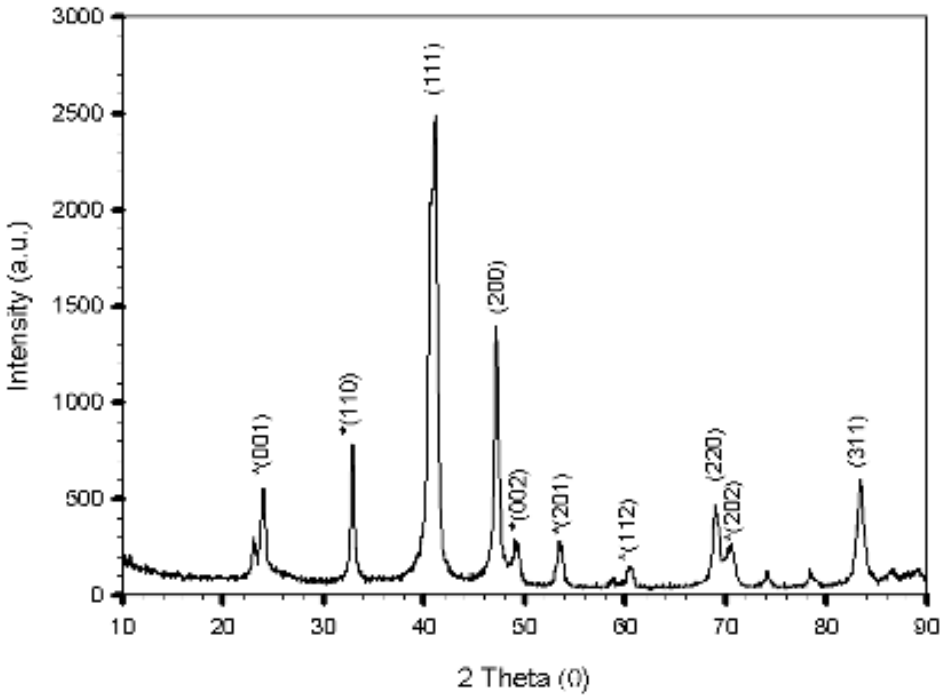


**Figure 11**. XRD pattern of $Pt_{56}Ni_8Fe_{36}$/C catalyst prepared by thermochemical treatment at 800°C under $H_2$.

Figure 12 compares the differences and similarities of these PtNiFe/C catalysts and the commercial Pt/C catalyst. To further investigate the peak shift of (111) and the appearance of the peak at 44.2°. Comparison of the XRD patterns of $Pt_{11}Ni_{18}Fe_{71}$/C, $Pt_{24}Ni_{45}Fe_{31}$/C, $Pt_{32}Ni_{30}Fe_{37}$/C, $Pt_{37}Ni_{36}Fe_{26}$/C, and $Pt_{56}Ni_8Fe_{36}$/C with commercial Pt/C was made, as shown in Figure 12A. Commercial platinum nanoparticles on carbon support exhibited a (111) diffraction peak at 39.9°. This peak corresponds to the fcc structure of platinum. The (111) diffraction peaks in Figure 12A b through f are exhibited at 41.1°, 41.3°, 41.2°, 42.0° and 41.1°. The increase in 2 theta is an indication that the distance between unit cells has shortened. Hence,

a decrease in lattice constant. This peak shift suggests that the PtNiFe NPs have formed an alloy.

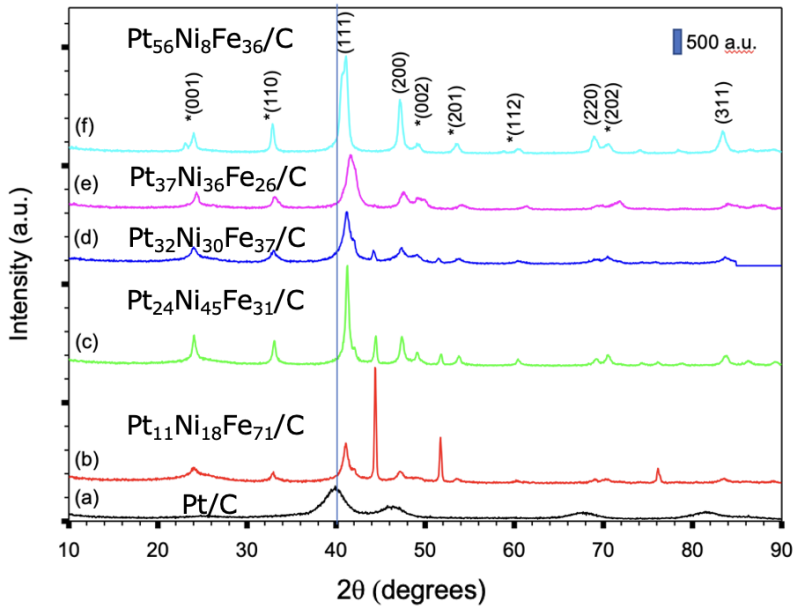


(A)

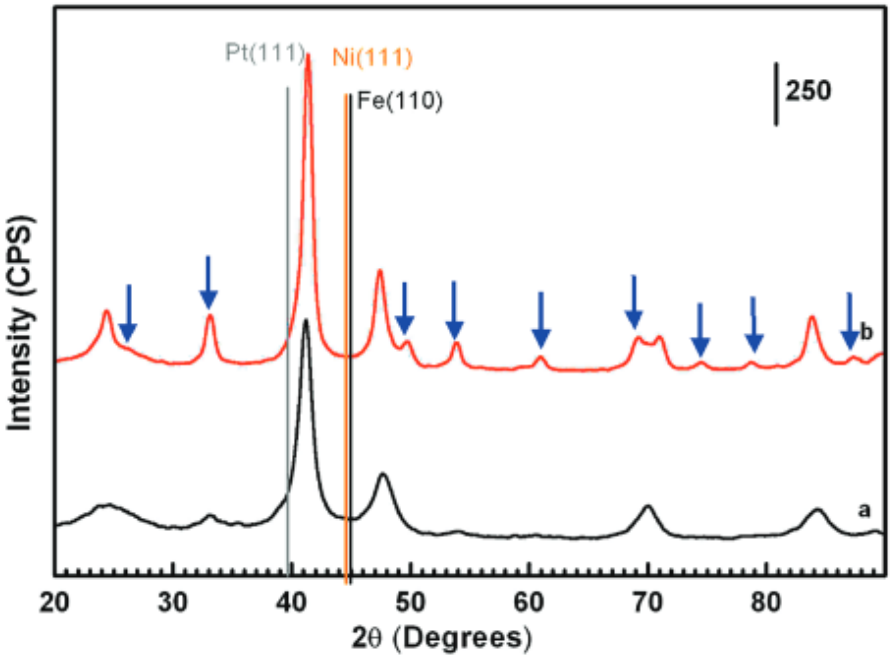


(B)

**Figure 12**. (A) XRD patterns of (a) commercial 40% Pt/C, (b) $Pt_{11}Ni_{18}Fe_{71}$/C, (c) $Pt_{24}Ni_{45}Fe_{31}$/C, (d) $Pt_{32}Ni_{30}Fe_{37}$/C, (e) $Pt_{37}Ni_{36}Fe_{26}$/C, and (f) $Pt_{56}Ni_{8}Fe_{36}$/C catalysts prepared by thermochemical treatment. (B) XRD patterns for $Pt_{46}Ni_{22}Fe_{32}$ catalyst synthesized by wet

chemical method and treated at different temperatures: 400 °C (a) and 800 °C (b). Blue arrows indicate the fct peaks in addition to the fcc diffraction peaks. [16].

The particularly strong peak at 44.2° in the diffraction pattern of $Pt_{11}Ni_{18}Fe_{71}$/C decreases as the platinum amount increases in the PtNiFe compositions, until the peak did not appear in the $Pt_{56}Ni_8Fe_{36}$/C diffraction pattern. Ni (111) peak occurs at 44.2° [17], whereas Fe (110) peak occurs at roughly 45.0°[18]. Thus, it is theorized that this strong peak at 44.2° may correspond to an aggregate of NiFe that was not alloyed successfully with platinum. It is also possible that some of the platinum was alloyed with these NiFe aggregates. Besides the low composition of platinum, this could also be due to the inconsistency from grinding the metal precursors by hand. In comparison, the diffraction pattern of $Pt_{46}Ni_{22}Fe_{32}$ synthesized from wet synthesis (Figure 12B) does not obtain a peak at 44.2°. The $Pt_{46}Ni_{22}Fe_{32}$ treated at 400 °C has a (111) diffraction peak located at 41.5°, while the one treated at 800 °C is located at 42.0°. In the $Pt_{46}Ni_{22}Fe_{32}$ treated at 800 °C, there are fct peaks that are exhibited at 24.5°, 33.0°, 49.0°, 53.0°, 74.0°, 78.5°, and 86.0°.This could either be contributed to consistency of the wet-chemical synthesis method, or the fairly high composition of platinum (46%) in these NPs.

Kuroki *et al.* found that when the Pt:M ratio is 3:1, 1:1, or 1:3, high-temperature treatment can induce a change in the crystal structure from a disordered fcc structure to an ordered fct structure, where platinum and nickel or iron are in alternating atomic planes [19].

Our group has previously synthesized PtNiFe via organic solvent with similar XRD results [16]. This is an indication that solid-state synthesis can achieve similar results compared to the organic wet synthesis method, while being more cost and time effective.

### 3.2.2 Lattice Constant Analysis

Utilizing the XRD patterns of the NPs obtained, the lattice constant was determined. Based on Bragg's law, the distance between the parallel plans of atoms, or the d-spacing can be determined. Equation 1 was first used to determine the d-spacing. Equation 2 was then used to determine the lattice constant at diffraction (111) peak, as shown in Table 2.

**Table 2**. Lattice constants calculated based on the (111) diffraction peak of the PtNiFe/C alloy catalysts.

| PtNiFe NPs | $Pt_{11}Ni_{18}Fe_{71}$ | $Pt_{24}Ni_{45}Fe_{31}$ | $Pt_{32}Ni_{30}Fe_{37}$ | $Pt_{37}Ni_{36}Fe_{26}$ | $Pt_{56}Ni_{8}Fe_{36}$ |
|---|---|---|---|---|---|
| Lattice Constant (Å) | 3.803 | 3.788 | 3.797 | 3.755 | 3.801 |

In comparison to the lattice constant of platinum, 3.924Å, the lattice constant of the NPs above has been shortened. This is due to the mixing of different size elements, as nickel and iron have lattice constants of 3.52 Å and 2.87 Å, respectively, which are smaller than the size of platinum (3.92 Å). Thus, a shortened lattice constant is an indicator of an alloy, corresponding to the XRD patterns from the previous section where the 111-peak shifted to a higher theta angle. As the nickel and iron are smaller in size than platinum, the distance between unit cell decreases for the 111 diffraction peaks. $Pt_{11}Ni_{18}Fe_{71}$/C has a small bump on

its 111-peak shoulder. This peak decreased as the platinum composition in the NPs increased, until it vanished at the 110-peak of $Pt_{56}Ni_8Fe_{36}$/C.

### 3.2.3 Domain Size Analysis

Besides being able to determine the lattice constant with the XRD patterns, the domain size can also be obtained. Domain size is the mean size of the ordered domains, which may be similar to particle size. Thus, this is merely a rough estimate of the particle size. The peak width in XRD patterns is related to the size of crystallites that compose the material. Based on the XRD patterns of the NPs displayed in section 3.2.1, the domain size was determined via Equation 3, as shown in Table 3.

**Table 3**. The calculated domain size of the NPs based on the XRD patterns

| PtNiFe NPs | $Pt_{11}Ni_{18}Fe_{71}$ | $Pt_{24}Ni_{45}Fe_{31}$ | $Pt_{32}Ni_{30}Fe_{37}$ | $Pt_{37}Ni_{36}Fe_{26}$ | $Pt_{56}Ni_8Fe_{36}$ |
|---|---|---|---|---|---|
| Domain size ($nm$) | 5.85 | 18.9 | 5.78 | 5.86 | 8.93 |

The particle size of the NPs is associated with the surface area of the catalyst. The smaller the particle size, the larger the surface area, thus increasing the catalytic ability. Based on the calculated domain size alone, the smallest NP is $Pt_{11}Ni_{18}Fe_{71}$, while the largest NP is $Pt_{24}Ni_{45}Fe_{31}$. As stated previously, the domain size is a good estimate of the particle size. To further determine the exact particle size of the NPs, other techniques such as TEM must be employed.

### 3.3.Fuel Cell Performance of Catalysts

After the physical characterizations of the NPs are analyzed, the catalytic performance of three catalysts with different platinum compositions were measured using a fuel cell testing station. MEAs were prepared using commercial 40 % Pt/C as the anode HOR catalyst, and PtNiFe/C were used for the cathode ORR catalyst. Due to the range of platinum loadings on the cathode, the data is normalized with regards to the total weight of platinum on the cathode. Figure 13 is a polarization curve showing the power density of MEA prepared with $Pt_{31}Ni_{27}Fe_{42}/C$ on the cathode with platinum loading at 0.0871 mg/cm$^2$. The current density is evaluated at 0.6V and determined to be 1.1 A cm$^{-2}$ mgpt$^{-1}$ and peak power density 0.8 W cm$^{-2}$ mgpt$^{-1}$ at a current density of 2.0 A cm$^{-2}$ mgpt$^{-1}$.

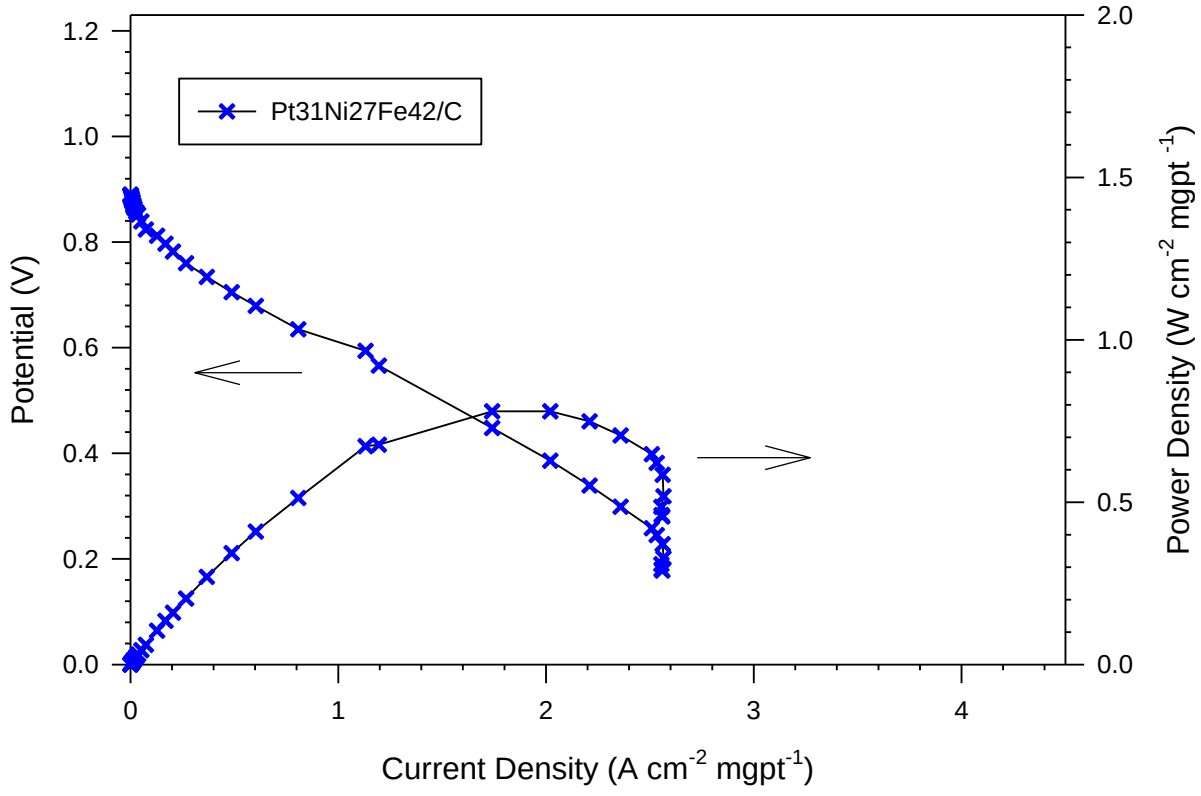

**Figure 13**. Polarization and power density curves of $Pt_{31}Ni_{27}Fe_{42}/C$ in PEMFC. Cell temperature maintained at 75°C with hydrogen and oxygen at 100% humidity at 65°C purged through the anode and cathode at 300scc/min and 150scc/min respectfully.

In order to better understand the effects of platinum composition on activity in a working fuel cell, the catalyst $Pt_{41}Ni_{31}Fe_{28}/C$ is evaluated in Figure 14. The cathode maintained a platinum load of 0.0806 mg/cm2. The polarization curve at 0.6V shows that $Pt_{41}Ni_{31}Fe_{28}/C$ has a current density of 2.4 A $cm^{-2}$ $mgpt^{-1}$ with a peak power density of $Pt_{41}Ni_{31}Fe_{28}/C$ is 1.4 W $cm^{-2}$ $mgpt^{-1}$ at current density 2.4 A $cm^{-2}$ $mgpt^{-1}$. This increase compared to $Pt_{31}Ni_{27}Fe_{42}/C$ demonstrates the impact the platinum concentration has on the performance in a fuel cell.

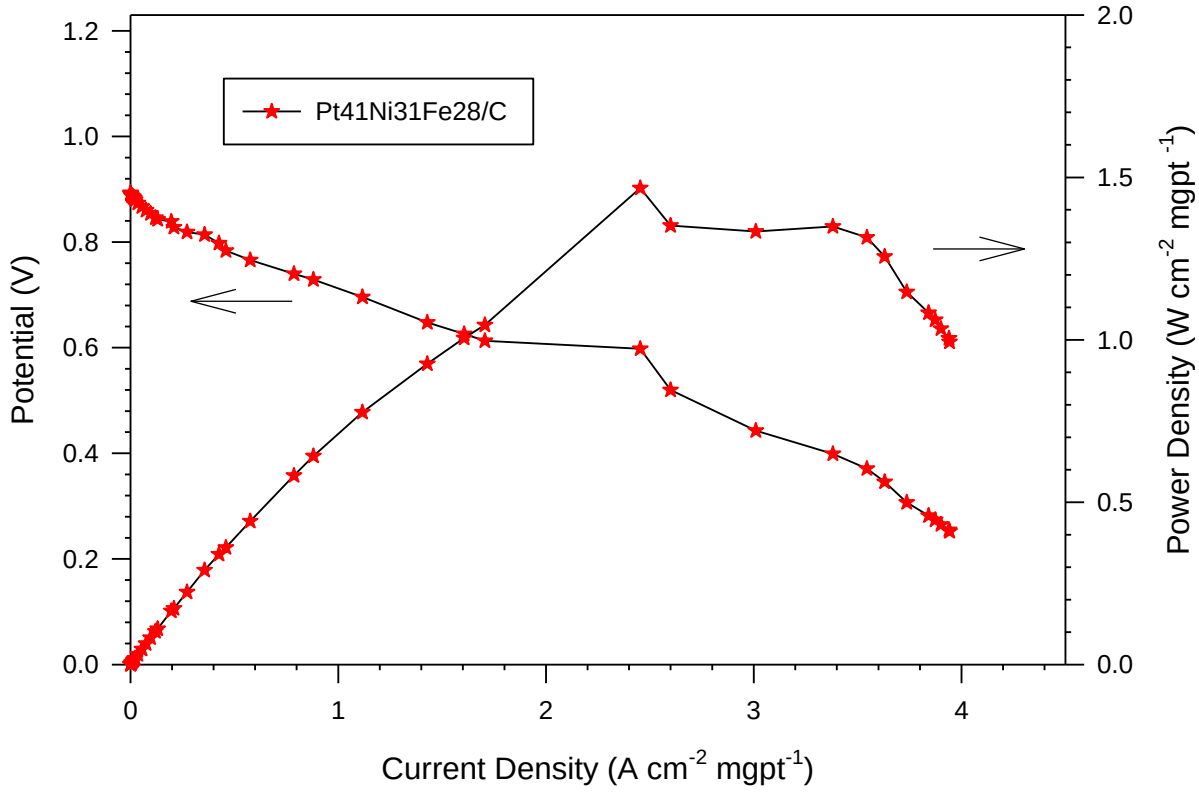

**Figure 14**. Polarization and power density curves of $Pt_{41}Ni_{31}Fe_{28}/C$ in PEMFC. Cell temperature maintained at 75°C with hydrogen and oxygen at 100% humidity at 65°C purged through the anode and cathode at 300scc/min and 150scc/min respectfully.

Continuing the comparison, the catalyst $Pt_{54}Ni_7Fe_{39}/C$ has the highest platinum composition with regards to $Pt_{31}Ni_{27}Fe_{42}/C$ and $Pt_{41}Ni_{31}Fe_{28}/C$ and has a platinum load of 0.1018 $mg/cm^2$. The polarization curve in Figure 15 for $Pt_{54}Ni_7Fe_{39}/C$ at 0.6 V has a current density of 2.0 A $cm^{-2}$ $mgpt^{-1}$. The power density is 1.2 W $cm^{-2}$ $mgpt^{-1}$ at 2.6 A $cm^{-2}$ $mgpt^{-1}$. This is the second highest current and power density of the three chosen catalysts despite the slightly higher loading, further demonstrating the significance the platinum composition has on the performance in a fuel cell. It is important to note that the nickel composition is much lower compared to the other two catalyst and could have also impacted the overall performance of the catalysts.

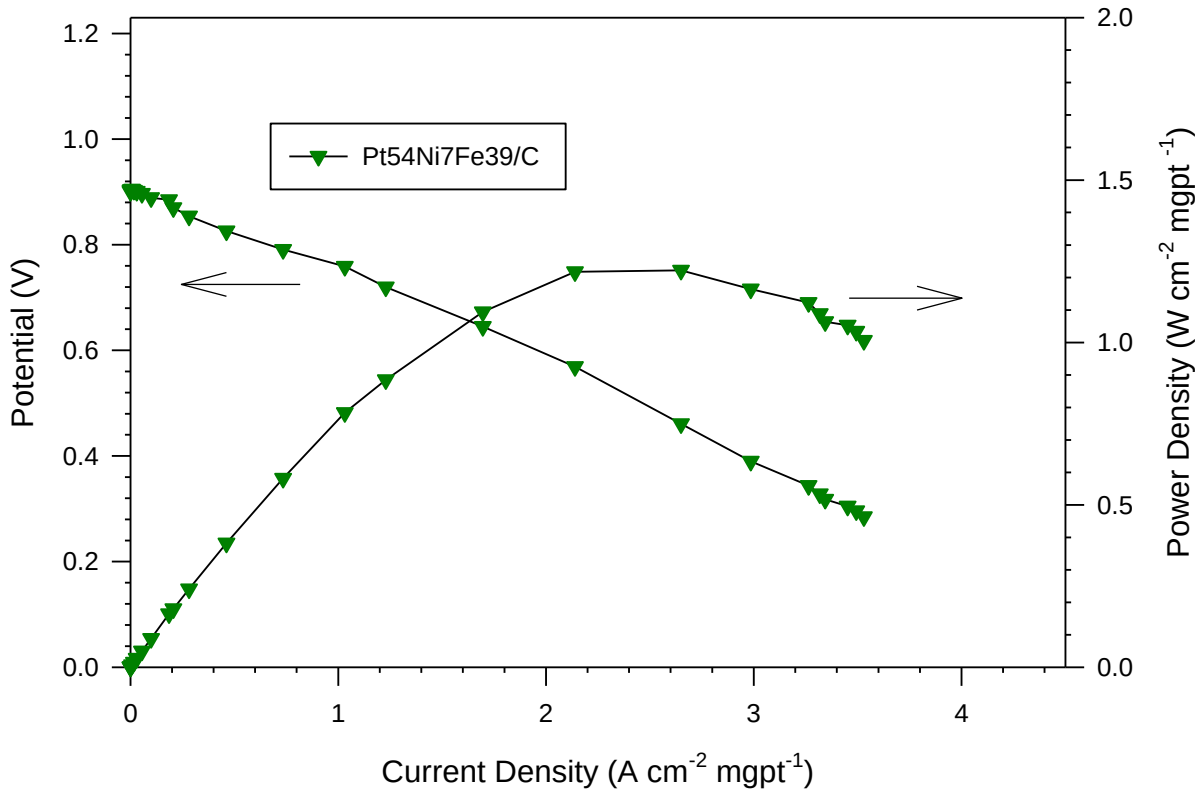


**Figure 15**. Polarization and power density curves of $Pt_{54}Ni_7Fe_{39}$/C in PEMFC. Cell temperature maintained at 75°C with hydrogen and oxygen at 100% humidity at 65°C purged through the anode and cathode at 300scc/min and 150scc/min respectfully.

Figure 16 compares the fuel cell performances of MEAs prepared from $Pt_{41}Ni_{31}Fe_{28}$/C, $Pt_{54}Ni_7Fe_{39}$/C, and $Pt_{31}Ni_{27}Fe_{42}$/C. The fuel cell performance data for the MEA prepared from commercial Pt/C catalyst is included for comparison. The polarization curve at 0.6 V for commercial Pt/C has a current density of 1.4 A $cm^{-2}$ $mgpt^{-1}$. Based on the performance of fuel cell voltage 0.6V, the pattern of current density as it relates to the PtNiFe composition is, $Pt_{54}Ni_7Fe_{39}$/C≥$Pt_{41}Ni_{31}Fe_{28}$/C≥Pt/C≥$Pt_{31}Ni_{27}Fe_{42}$/C. The power density is also mapped out

for comparison with commercial Pt/C against PtNiFe/C. The peak power density of Pt/C is 0.9 W $cm^{-2}$ $mgpt^{-1}$ at a current density of 1.9 A $cm^{-2}$ $mgpt^{-1}$. Based on this preliminary work, the catalytic performance of $Pt_{54}Ni_7Fe_{39}$/C and $Pt_{41}Ni_{31}Fe_{28}$/C are superior to Pt/C with the performance of $Pt_{31}Ni_{27}Fe_{42}$/C being slightly weaker. This is an indication that the addition of nickel and iron to platinum not only reduces the cost, but it can also increase its catalytic activity. This is also a demonstration that the solid-state synthesis method is capable of producing catalysts with superior catalytic activity.

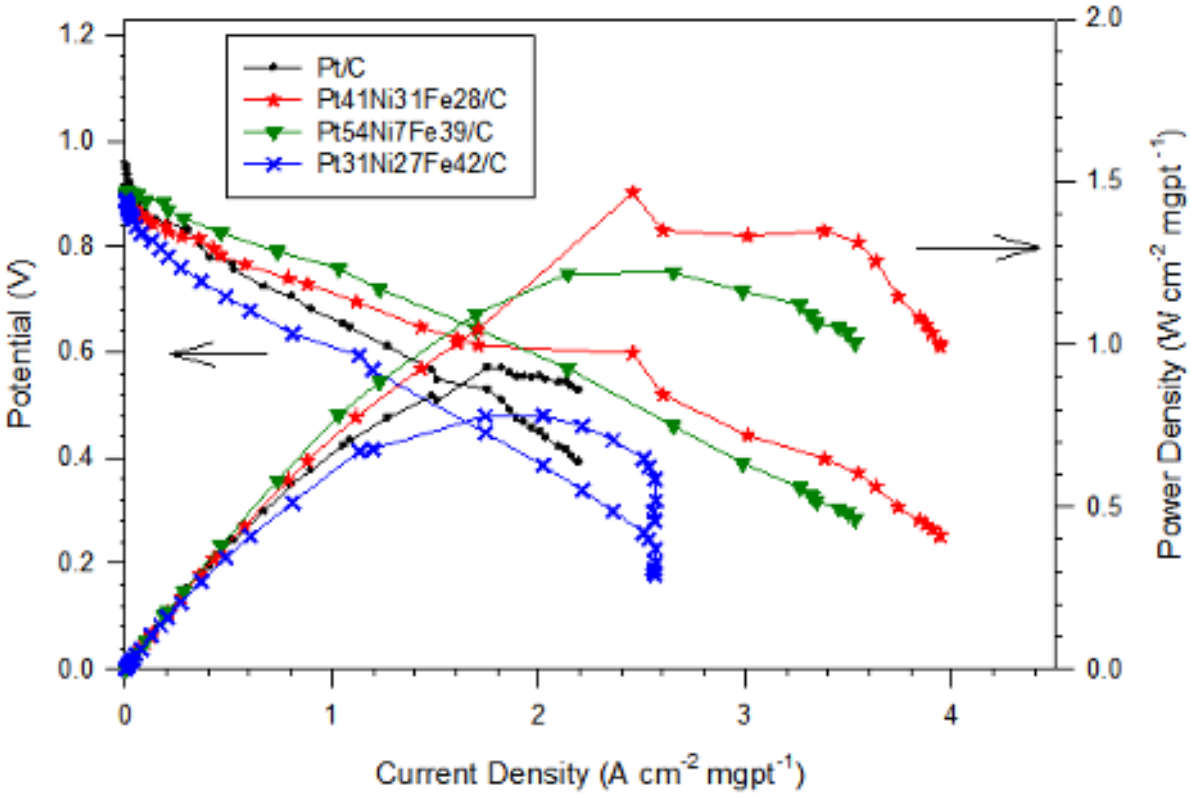


**Figure 16**. Comparison of the polarization and power density curves of MEAs with cathodes loaded with Pt/C, $Pt_{41}Ni_{31}Fe_{28}$/C, $Pt_{54}Ni_7Fe_{39}$/C, $Pt_{31}Ni_{27}Fe_{42}$/C, and Pt/C in PEMFC at 75°C. Anode and cathode metal loading was maintained from 0.1 mg/$cm^2$ – 0.2 mg/$cm^2$.

The superior fuel cell performance of these NPs and their physical characteristics, which are like the NPs synthesized through wet synthesis method, provide promising insight on the potential of the solid-state synthesis method. This solid-state synthesis technique has the potential to further reduce cost of the catalyst as it removes the need for costly organic solvents and does not require additional steps to be placed on the supporting substrate.

## 4. CONCLUSIONS

The results from ICP-OES indicated that the calculated molar feed ratio of the metals aligned closely with the actual composition in the NPs, forming a linear regression of $y = 0.9982x + 0.0588$ with an $R^2$ value of 0.9801. The NPs exhibited fcc structure and fct structure in the XRD patterns. $Pt_{11}Ni_{18}Fe_{71}/C$, $Pt_{24}Ni_{45}Fe_{31}/C$, and $Pt_{32}Ni_{30}Fe_{37}/C$ exhibited phase segregation of nickel and iron. This issue was resolved as the platinum composition increased. The lattice constant of the PtNiFe NPs presented were smaller than the lattice constant of platinum (111) fcc peak. The domain size of the NPs was relatively small, ranging from 5 nm to 18 nm. From the preliminary fuel cell performance test, $Pt_{54}Ni_{7}Fe_{39}/C$ and $Pt_{41}Ni_{31}Fe_{28}/C$ demonstrated to have superior catalytic performance compared to Pt/C. Alloying iron and nickel with platinum not only reduces the production cost, but it also can increase its catalytic performance. The solid-state synthesis method produced similar results to the wet synthesis of PtNiFe, but it eliminated the organic waste produced. Thus, the solid-

state synthesis is a technique for NP synthesis that has promise to reduce the cost of platinum-based catalysts and maintain high catalytic activity for ORR in fuel cells.

## 5. FUTURE WORK

One problem in the NP synthesis procedure presented in this thesis is the homogeneity in terms of precursor dispersion and distribution. The incorporation of a ball mill for future experiments could increase the consistency of this aspect. Due to time constraints, more TEM analyses of these PtNiFe NPs have yet to be taken. As the domain size obtained from the XRD data is an estimate of the particle size, further techniques, like TEM, need to be conducted to determine the accurate particle size of NPs as well as geometric shape. Furthermore, more fuel cell testing is required, such as the determination of mass activity or electrochemically active surface area using cyclic voltammetry techniques.

## 6. REFERENCES


[1] Alvarez-Meaza, I.; Zarrabeitia-Bilbao, E.; Rio-Belver, R.M.; Garechana- Anacabe, G. Fuel-Cell Electric Vehicles: Plotting a Scientific and Technological Knowledge Map. *Sustainability* **2020**, *12*, 2334. https://doi.org/10.3390/su12062334

[2] EPA, U.S.; OAR. Sources of Greenhouse Gas Emissions. **2015**. https://www.epa.gov/ghgemissions/sources-greenhouse-gas-emissions

[3] U.S. petroleum consumption decreased to a 25-year low in 2020 https://www.eia.gov/todayinenergy/detail.php?id=49016 (accessed 2022 -04 -30).

[4] Cano, Z. P.; Banham, D.; Ye, S.; Hintennach, A.; Lu, J.; Fowler, M.; Chen, Z. Batteries and Fuel Cells for Emerging Electric Vehicle Markets. *Nat. Energy* **2018**, *3*(4), 279–289. https://doi.org/10.1038/s41560-018-0108-1

[5] Zhong, C.-J.; Luo, J.; Njoki, P. N.; Mott, D.; Wanjala, B.; Loukrakpam, R.; Lim, S.; Wang, L.; Fang, B.; Xu, Z. Fuel Cell Technology: Nano-Engineered Multimetallic Catalysts. *Energy Environ. Sci.* **2008**, *1* (4), 454–466. https://doi.org/10.1039/B810734N.

[6] Ning, F.; He, X.; Shen, Y.; Jin, H.; Li, Q.; Li, D.; Li, S.; Zhan, Y.; Du, Y.; Jiang, J.; Yang, H.; Zhou, X. Flexible and Lightweight Fuel Cell with High Specific Power Density. *Acs Nano 2017. 11 (6),* 5982-5991

[7] Holton, O. T.; Stevenson, J. W. The Role of Platinum in Proton Exchange Membrane Fuel Cells. *Platin. Met. Rev.* **2013**, *57* (4), 259–271. doi:10.1595/147106713x671222

[8] Whiston, M. M.; Azevedo, I. L.; Litster, S.; Whitefoot, K. S.; Samaras, C.; Whitacre, J. F. Expert Assessments of the Cost and Expected Future Performance of Proton Exchange Membrane Fuel Cells for Vehicles. *Proc. Natl. Acad. Sci. U. S. A.* **2019**, *116* (11), 4899–4904.https://doi.org/10.1073/pnas.1804221116

[9] Neto, V. Nanoparticle synthesis. https://www.nanoscience.com/techniques/nanoparticle-synthesis/ (accessed 2022 -04 -11).

[10] Gao, S.; Hao, S.; Huang, Z.; Yuan, Y.; Han, S.; Lei, L.; Zhang, X.; Shahbazian-Yassar, R.; Lu, J. Synthesis of High-Entropy Alloy Nanoparticles on Supports by the Fast Moving

Bed Pyrolysis. *Nat. Commun.* **2020**, *11* (1), 2016. https://doi.org/10.1038/s41467-020-15934-1.

[11] Sarkar, S.; Ramarao, S. D.; Das, T.; Das, R.; Vinod, C. P.; Chakraborty, S.; Peter, S. C. Unveiling the Roles of Lattice Strain and Descriptor Species on Pt-like Oxygen Reduction Activity in Pd–Bi Catalysts. *ACS Catal.* **2021**, *11* (2), 800–808. https://doi.org/10.1021/acscatal.0c03415.

[12] Kareem, H.; Maswadeh, Y.; Wu, Z.-P.; Leff, A. C.; Cheng, H.-W.; Shan, S.; Wang, S.; Robinson, R.; Caracciolo, D.; Langrock, A.; Mackie, D. M.; Tran, D. T.; Petkov, V.; Zhong, C.-J. Lattice Strain and Surface Activity of Ternary Nanoalloys under the Propane Oxidation Condition. *ACS Appl. Mater. Interfaces* **2022**, *14* (9), 11435–11447. https://doi.org/10.1021/acsami.1c24007.

[13] Wanjala, B. N.; Loukrakpam, R.; Luo, J.; Njoki, P. N.; Mott, D.; Zhong, C.-J.; Shao, M.; Protsailo, L.; Kawamura, T. Thermal Treatment of PtNiCo Electrocatalysts: Effects of Nanoscale Strain and Structure on the Activity and Stability for the Oxygen Reduction Reaction. *J. Phys. Chem. C Nanomater. Interfaces* **2010**, *114* (41), 17580–17590. https://doi.org/10.1021/jp106843k.

[14]. Shan, S.; Petkov, V.; Yang, L.; Mott, D.; Wanjala, B. N.; Cai, F.; Chen, B. H.; Luo, J.; Zhong, C.-J. Oxophilicity and Structural Integrity in Maneuvering Surface Oxygenated Species on Nanoalloys for CO Oxidation. *ACS Catal.* **2013**, *3* (12), 3075–3085. https://doi.org/10.1021/cs400700r.

[15] Wu, J.; Shan, S.; Luo, J.; Joseph, P.; Petkov, V.; Zhong, C.-J. PdCu Nanoalloy Electrocatalysts in Oxygen Reduction Reaction: Role of Composition and Phase State in Catalytic Synergy. *ACS Appl. Mater. Interfaces* **2015**, *7* (46), 25906–25913. https://doi.org/10.1021/acsami.5b08478.

[16] Wanjala, B. N.; Fang, B.; Luo, J.; Chen, Y.; Yin, J.; Engelhard, M. H.; Loukrakpam, R.; Zhong, C.-J. Correlation between Atomic Coordination Structure and Enhanced Electrocatalytic Activity for Trimetallic Alloy Catalysts. *J. Am. Chem. Soc.* **2011**, *133*(32), 12714–12727. https://doi.org/10.1021/ja2040464.

[17] Borges, R. P.; Ribeiro, B.; Cruz, M. M.; Godinho, M.; Wahl, U.; da Silva, R. C.; Gonçalves, A. P.; Magén, C. Nanoparticles of Ni in ZnO Single Crystal Matrix. *Eur. Phys. J. B* **2013**, *86* (6). https://doi.org/10.1140/epjb/e2013-40008-5

[18] Singh, S.; Basu, S.; Gupta, M.; Vedpathakz, M.; Kodama, R. H. Investigation of Interface Magnetic Moment of Fe⁄Ge Multilayer: A Neutron Reflectivity Study. *J. Appl. Phys.* **2007**, *101* (3), 033913. https://doi.org/10.1063/1.2450680.

[19] Kuroki, H.; Tamaki, T.; Matsumoto, M.; Arao, M.; Kubobuchi, K.; Imai, H.; Yamaguchi, T. Platinum–Iron–Nickel Trimetallic Catalyst with Superlattice Structure for Enhanced Oxygen Reduction Activity and Durability. *Ind. Eng. Chem. Res.* **2016**, *55* (44), 11458–11466. https://doi.org/10.1021/acs.iecr.6b02298.

## 7. ACKNOWLEDGMENTS

I would like to thank my advisor, Dr. Zhong, my committee members, Dr. Zhong, Dr. Lees, and Dr. Swierk. I would also like to thank my graduate student Dominic Caracciolo for his guidance and help over the past year and a half. I would also like to thank Rick Robinson, Merry Madiou, Justine Gordon, Claudia Cheung and all the graduate students in the Zhong lab for their help.

I would like to acknowledge Dr. David Jenkins, Michael Colwell and David Collins for their assistance with XRD and ICP measurements.

I would like to thank the Binghamton University Research Foundation for their support of my work through the Undergraduate Award to Support Research and Creative Work.